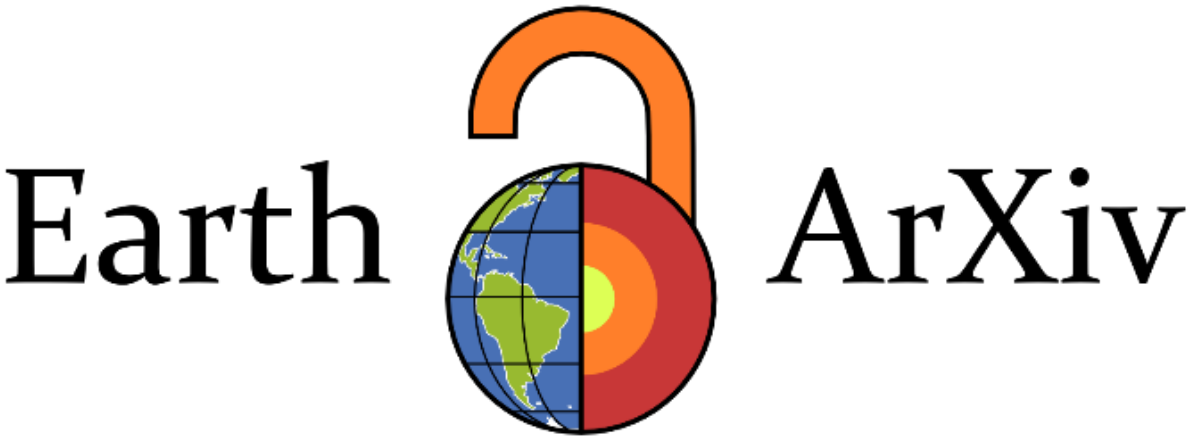

Agricultural Fallowing Drives Extreme Anthropogenic Dust and Visibility Degradation During the October 2021 Dust Event in California's Central Valley

Yang Yu[1,2], Shu-Hua Chen[2], Adeyemi A. Adebiyi[3], Md. Minhazul Kibria[3], Satyendra Pandey[3].

[1] Woods Hole Oceanographic Institution, Woods Hole, MA, USA

[2] Department of Land, Air and Water Resources, University of California, Davis, CA

[3] Department of Life and Environmental Sciences, University of California Merced, Merced, CA

Correspondence to: Yang Yu and Shu-Hua Chen, yang.yu@whoi.edu; shachen@ucdavis.edu

Abstract

Anthropogenic dust aerosols from agricultural land affect regional air quality, visibility, and radiation, yet they are often ignored in atmospheric models. Here, we investigate the role of fallow croplands in driving anthropogenic dust emissions during the October 11, 2021, wind-driven dust event over California's Central Valley (CV). The simulation without fallow croplands fails to reproduce the dust event, whereas the simulation including fallow-induced erodibility produces 90 t of dust emissions, reproducing the observed aerosol optical depth of 0.6-0.8 and PM_{10} concentrations of 1000-1200 μg m^{-3}. Fallow-land-emitted dust reduces surface net radiation by 30 W m^{-2}, leading to near-surface cooling of 0.2 °C and degraded visibility up to 1000 m. These results highlight the important role of agricultural fallowing in regulating regional dust emissions, particularly as climate-driven drought and groundwater sustainability policy are projected to substantially expand fallowed cropland areas across the CV in the coming decades.

Key Points

- Fallow croplands contributed to major anthropogenic dust emissions during the October 2021 dust event in California's Central Valley.
- Including fallow land erodibility enables WRF-Chem to reproduce observed aerosol optical depth and extreme PM_{10} concentrations.
- Dust from fallow croplands reduced surface net downward solar radiation and degraded regional visibility.

Plain Language Summary

Windblown dust from agricultural land can strongly affect air quality, visibility, and climate, but it is often poorly represented in atmospheric models. In California's Central Valley, large areas of farmland were left fallow during the severe 2021 drought, leaving bare soil that can easily emit dust when strong winds occur. On October 11, 2021, a major wind event generated widespread dust plumes across the region. In this study, we used a high-resolution atmospheric model to examine how fallow croplands contributed to this dust event. By using satellite observations to identify exposed farmland, we improved the model representation of dust emissions. The model simulations show that fallow croplands were responsible for large amounts of dust during the event, leading to severe air pollution and reduced visibility. The dust also reduced sunlight reaching the surface and slightly cooled near-surface temperatures. These results highlight the important role of agricultural land management in controlling dust emissions and their environmental impacts, particularly as climate-driven drought and groundwater sustainability policy, such as the Sustainable Groundwater Management Act (SGMA), are projected to substantially expand fallowed cropland areas across the Central Valley in the coming decades.

1. Introduction

Anthropogenic dust is an important contributor to particulate matter in semi-arid regions, particularly in intensively managed agricultural regions where land surface properties are strongly shaped by human activities (Chen et al., 2023; Ginoux et al., 2012; Webb & Pierre, 2018). Unlike natural desert dust, anthropogenic dust emissions are highly sensitive to short-term variations in surface roughness, vegetation cover, and soil exposure, and can respond rapidly to the changes in wind forcing (Huang et al., 2015; Prospero et al., 2002; Tegen & Fung, 1995; Xi & Sokolik, 2016; Zender et al., 2004). As a result, episodic wind events can trigger sharp increases in anthropogenic dust aerosol concentrations on short timescales of hours to days. Yet despite growing recognition of anthropogenic dust as an important aerosol source, its representation in atmospheric models remains poor, and its contributions to extreme air quality events, visibility, and regional radiative balance are systematically underestimated (e.g., Kok et al., 2025).

Windblown anthropogenic dust aerosols affect air quality and visibility, posing substantial risks to public health and safety, including disease and elevated rates of traffic accidents (Bhattachan et al., 2019; Ostro et al., 2021). For example, reduced visibility during dust events has been directly linked to increased collision rates and fatal traffic accidents on highways traversing agricultural regions (Bhattachan et al., 2019; Tong et al., 2023). In addition, dust exposure has also been associated with increased respiratory and cardiovascular morbidity (Dominski et al., 2021; Goudie, 2014). In the western United States, exposure to anthropogenic dust is linked to the spread of dust-borne pathogens, including Coccidioides spp. fungal spores, which contribute to the rising incidence of coccidioidomycosis (Valley fever) (Centers for Disease Control and Prevention (CDC), 2013; Cooksey et al., 2020; Tong et al., 2017). Beyond air quality and health impacts, anthropogenic dust aerosols can also absorb and scatter solar radiation, perturb surface energy balance, and modify atmospheric heating rates, thereby influencing near-surface winds, heat extremes, and regional hydroclimate (Kok et al., 2023; Miller & Tegen, 1998; Stanelle et al., 2014).

Despite these impacts, quantifying the contribution of anthropogenic dust to atmospheric aerosol loading remains challenging, particularly at event scales, and is often ignored in regional and climate models (Evans et al., 2016; Shevliakova et al., 2024). For example, source attribution based on observations in regions where multiple source types coexist is difficult, complicating regional air quality assessments (Ginoux et al., 2012; Philip et al., 2017). Although satellite remote

sensing has been widely used to detect dust activity and identify potential source regions (Baddock et al., 2016; Ginoux et al., 2010; Hsu et al., 2013), attribution based on static land-use classifications may overlook short-term land management practices and surface conditions that directly regulate soil erodibility (Webb & Pierre, 2018). Specifically, most dust emission schemes employed in regional and climate models rely on representations of land surface properties that are updated infrequently and therefore cannot capture the rapid, seasonal transitions in surface erodibility (Zender et al., 2004). These limitations contribute to uncertainties in simulated anthropogenic dust emissions and their associated radiative effects, particularly under warming and drying climate conditions that can exacerbate the seasonal surface transitions (Kok et al., 2023; Mahowald & Luo, 2003).

One of the regions where the difficulty of simulating anthropogenic dust is more visible than in others is California's Central Valley (CV). The CV is one of the most productive agricultural regions in the world and a well-documented hotspot for anthropogenic dust emissions (Adebiyi et al., 2025; Ginoux et al., 2012). Its flat terrain, extensive cropland coverage, and frequent stagnation conditions make air quality in the CV particularly sensitive to land-use disturbances. Agricultural land management in the CV strongly regulates soil moisture, vegetation cover, and surface erodibility, thereby controlling the sensitivity of croplands to wind-driven dust emissions (Baker et al., 2005; Pu et al., 2022). In addition, climate-driven drought can influence land management, resulting in the fallowing of agricultural lands - a practice in which agricultural lands are intentionally left uncultivated for one or more growing seasons (Espinoza et al., 2023; Plassin et al., 2021). Previous studies have shown that the CV accounts for the majority of the total fallowed land areas in California, and these fallowed lands are associated with about 88% of major anthropogenic dust sources over the region (Adebiyi et al., 2025). These fallowed fields are characterized by reduced soil moisture, diminished vegetation cover, and elevated surface temperatures relative to actively cultivated croplands, rendering them highly susceptible to wind erosion (Adebiyi et al., 2025). Despite their occurrence, these fallowed lands are frequently not accounted for in models, making it difficult to assess the impacts of associated anthropogenic dust events on air quality and energy balance in the CV.

For example, the year 2021 was characterized by severe drought across California, resulting in extensive agricultural fallowing of approximately 3,232 km^2 in the CV (Adebiyi et al., 2025).

During a synoptic-scale wind event on October 11, 2021, sustained near-surface strong winds coincided with pronounced increases in airborne particulate matter (Ebiendele et al., 2026). Wind gusts exceeding 40 mph (17.8 m/s) generated widespread blowing dust across the CV, reducing visibility to near-zero levels. The high-wind event caused widespread societal and infrastructure disruptions, including precautionary power shutoffs, numerous downed trees and power lines, freeway closures due to blowing dust and reduced visibility, and several wind-driven fires across the region. Satellite imagery and surface observations revealed extensive dust plumes originating from agricultural areas during the event. However, it remains unclear whether drought-driven fallow croplands acted as a major anthropogenic dust source during the event (Adebiyi et al., 2025).

To fill this gap, we investigate the role of fallow croplands in driving anthropogenic dust emissions, using the October 11, 2021, dust event as a case study. We use 1.3-km-resolution simulations with the Weather Research and Forecasting model coupled with Chemistry (WRF-Chem), and explicitly represent fallow croplands in the dust emission scheme to quantify their contributions to dust aerosol loading, air quality degradation, and perturbations to the local radiative balance. Our results not only demonstrate that a spatially limited area of fallowed cropland can become the dominant regional dust source during strong wind events but also provide quantitative assessments of the radiative and air quality consequences of agricultural fallowing.

2. Data and Methods

2.1 Model Configuration

WRF-Chem simulations with the Goddard Chemistry Aerosol Radiation and Transport (GOCART) simple aerosol scheme (chem_opt=300) were conducted to investigate the October 11, 2021, wind-driven dust event over California's CV. The simulations were performed using WRF version 4.6.1. Figure 1a shows the model domains used in this study. The model was configured with three two-way nested domains (d01-d03) with horizontal resolutions of 12, 4, and 1.333 km, and domain sizes of 240×240, 421×421, and 661×661 grid points, respectively. The innermost domain (d03) covers the entire CV, allowing explicit representation of fine-scale land surface heterogeneity relevant to dust emission. In the vertical direction, the model has 60 terrain-following levels with enhanced resolution near the surface, and the model top is set at 100 hPa. The simulation was integrated for two days, from 00 UTC 11 October 2021 to 00 UTC 13 October 2021, covering the full high-wind event from 06 PST to 18 PST on 11 October.

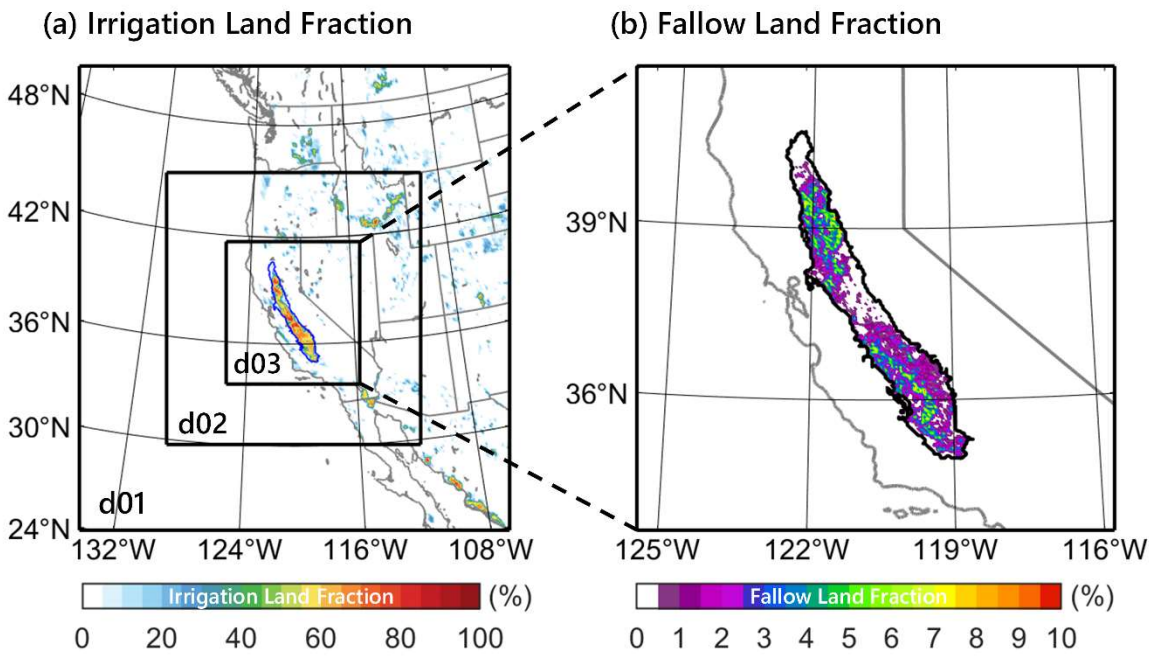

Figure 1. (a) Model domain and agriculture irrigation land fraction, and (b) fallow land fraction in California's Central Valley derived from satellite Normalized Difference Vegetation Index (NDVI) observations.

The model's physical parameterizations are described in Text S1. Windblown dust emissions in the model were simulated using the Air Force Weather Agency (AFWA) dust emission scheme (LeGrand et al., 2019), in which dust emissions are controlled by near-surface wind speed, soil clay fraction, and surface erodibility. The bulk dust emission flux is calculated as:

$$F_{bulk} = G\alpha \times Erod, \quad (1)$$

where F_{bulk} is the bulk dust emission flux triggered by saltation; G is the saltation flux calculated following Marticorena & Bergametti (1995); $\alpha = 10^{0.134(C_s)-6}$ is the emission efficiency factor that depends on the soil clay fraction C_s; and $Erod$ is the fractional erodible area of each grid cell, ranging from 0 to 1.

2.2 Fallow Land Fraction and Erodibility Formulation

Fallow croplands in California's CV are identified by combining the high-resolution United States Department of Agriculture (USDA) Crop Data Layer (CDL) with satellite-derived Normalized Difference Vegetation Index (NDVI) data to represent land surface conditions immediately prior

to the October 2021 dust event. Details of the method are provided in Text S2. We combined the fallowed cropland information with 30-m-resolution NDVI observations acquired on 25 September 2021 and 3 October 2021, corresponding to the most recent available observations before the event. Because neither the 25 September 2021 nor the 3 October 2021 individually provided complete spatial coverage of the CV, NDVI fields from the two dates were averaged to obtain spatially continuous regional coverage.

The NDVI-derived fallow land fraction F_{fallow} was incorporated into the AFWA dust emission scheme by modifying the surface erodibility:

$$Erod = Erod_{\text{original}} + F_{fallow} \quad (2)$$

where $Erod_{\text{original}}$ represents the baseline erodibility associated with soil and land-surface properties in the standard AFWA scheme, and F_{fallow} accounts for enhanced surface exposure due to agricultural fallowing. This formulation extends the AFWA representation of surface erodibility without altering other components of the dust emission framework. All remaining dust emission parameters, including soil texture, clay fraction, and wind-driven saltation flux, were held constant across experiments.

2.3 Experimental Design

To isolate the contribution of fallow croplands to anthropogenic dust emissions during the October 2021 dust event, we conducted a pair of numerical experiments that differ only in the treatment of fallow-land erodibility. In the control experiment (CTRL), surface erodibility follows the standard AFWA dust emission formulation without any additional contribution from fallow croplands. In the sensitivity experiment (FLDUST), the NDVI-derived fallow land fraction is incorporated into the surface erodibility parameter, allowing fallowed agricultural land to contribute to wind-driven dust emissions. The fractional percentages of erodible fallowed land per grid box ranged up to 10% in some locations and averaged about 2% during October 2021 (Fig. 1b). By comparing these two experiments, we quantify the impact of agricultural fallowing on dust aerosol loading, air quality, and associated radiative effects.

3. Results and Discussion

3.1 Event Overview and Model Evaluation

The October 11, 2021, dust event over California's CV was associated with a synoptic-scale wind event that generated sustained enhancements in near-surface winds. The CV is bounded by the Sierra Nevada and Coast Ranges, which usually favor locally driven circulations and limit surface wind speeds. The October 2021 wind event was associated with an unusual deep midlatitude trough, located to the east of the surface high, over the western United States, which generated a strong surface pressure gradient across California, resulting in strong near-surface winds.

Observations from automatic surface meteorological stations of the National Weather Service (NWS) Automated Surface Observing System (ASOS) show that strong winds over the CV persisted from 06:00 to 18:00 PST (Fig. S1). These prolonged winds may activate exposed fallow croplands as major anthropogenic dust sources, leading to substantial dust emissions (Adebiyi et al., 2025). Figure 2a shows satellite-observed aerosol optical depth (AOD) over the CV at around 13:00 PST. The AOD was derived from merged products of the Moderate Resolution Imaging Spectroradiometer (MODIS) from Satellites Terra and Aqua, and the Visible Infrared Imaging Radiometer Suite (VIIRS) from Satellites Suomi National Polar-orbiting Partnership (Suomi NPP) and National Oceanic and Atmospheric Administration (NOAA)-20. The observed AOD ranges from 0.6 to 0.8 across most of the southern CV. In the meantime, monitoring stations operated by the United States Environmental Protection Agency (EPA) also reported extreme PM_{10} (particulate matter with aerodynamic diameters generally 10 μm or smaller) concentrations over the southern CV, with observed PM_{10} concentrations ranging from 1000 to 1200 μg m^{-3} (Fig. 2d).

The model successfully reproduces the observed surface wind variations during the wind event, capturing the timing and magnitude of wind enhancement over the CV (Fig. S1). The simulation indicates that the wind event began between 06:00 and 07:00 PST, with peak wind speeds of 16 to 18 m s^{-1} over the northern CV from 08:00 to 10:00 PST. Strong winds subsequently expanded southward between 11:00 and 16:00 PST and weakened rapidly after 17:00 PST, with the event ending at 18:00 PST (Fig. S1). Given the realistic representation of synoptic-scale wind forcing, differences in simulated aerosol loading primarily reflect the model's treatment of dust emissions. In CTRL, almost no dust aerosol loading is produced over the CV, with dust AOD remaining near zero across most of the region (Fig. 2b), and simulated surface PM_{10} concentrations remaining negligible (Fig. 2e), failing to reproduce the satellite-observed AOD and the extreme PM_{10} concentrations measured at EPA monitoring stations. Almost all the simulated dust in CTRL is

over the Mojave Desert and southeastern California. In contrast, when fallow-induced erodibility is included, the FLDUST produces substantial increases in both dust AOD and PM_{10} across the CV (Figs. 2c and 2f). Although the simulated AOD and PM_{10} maxima at 13:00 PST are displaced slightly north of the observed locations (Figs. 2a, 2c, 2d, and 2f), this discrepancy is likely related to a delay in the simulated southward expansion of strong winds, made difficult by the topographic features surrounding the CV (Fig. S1). The FLDUST successfully reproduces the satellite-observed AOD magnitude of 0.6-0.8 and the extreme PM_{10} concentrations of 1000-1200 µg m^{-3} over the CV. These results provide strong evidence that dust emissions from fallow croplands over the CV were the dominant source during the October 11, 2021, dust event, and were missed by the default model configuration.

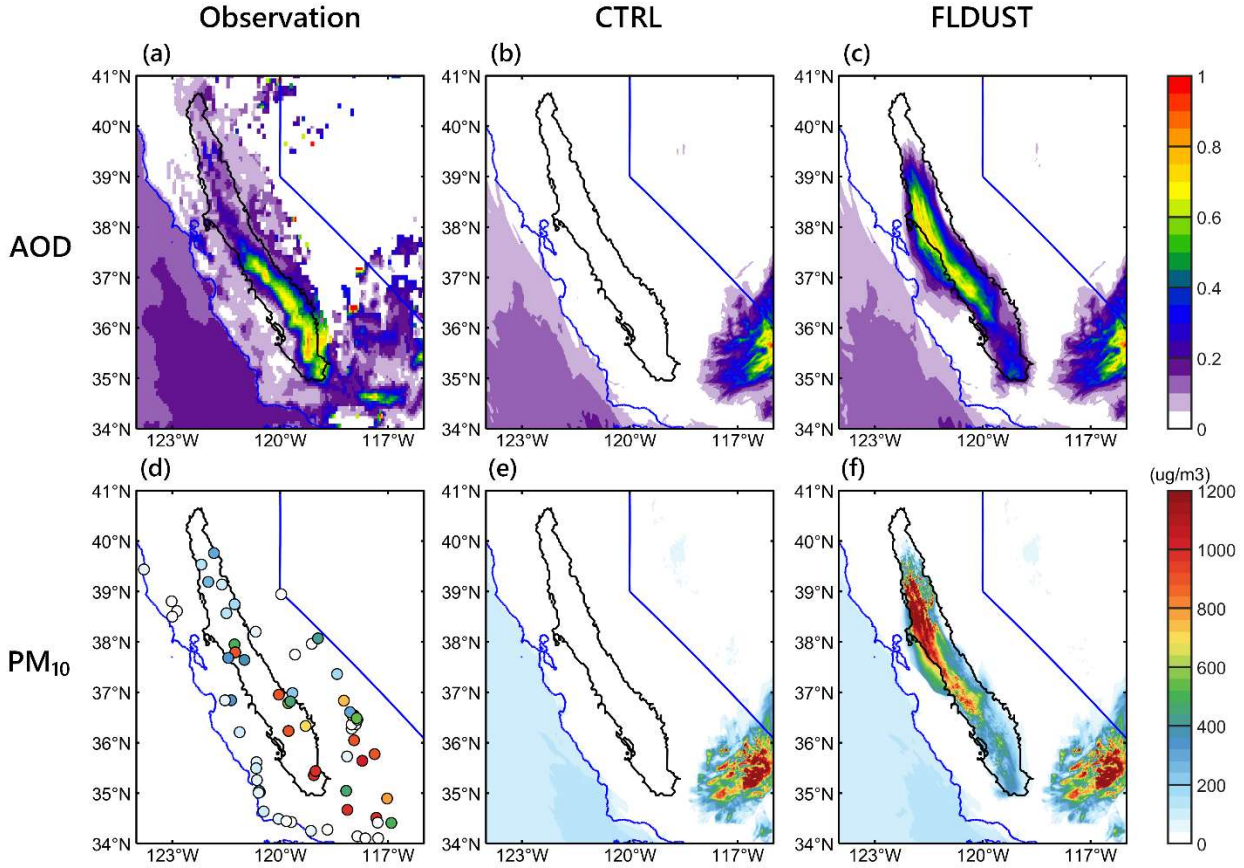

Figure 2. (a) Satellite-observed aerosol optical depth (AOD); WRF-Chem simulated dust AOD from (b) CTRL and (c) FLDUST; (d) PM_{10} observations at EPA monitoring stations; and simulated PM_{10} from (e) CTRL and (f) FLDUST. Both the observations and model results are shown at the satellite overpass time of 13:00 PST, October 11, 2021.

3.2 Enhancement of Dust Emissions and Radiative Effects

Including fallow croplands as erodible surfaces significantly increases simulated dust emissions during the October 11, 2021, dust event (Fig. 2). Figure 3a shows the temporal evolution of regional-averaged dust emissions and atmospheric dust loading in FLDUST over the CV. Dust emissions increase rapidly after the strong surface winds onset at 06:00 PST, with the maximum emission rate of 9-10 t h^{-1} between 09:00 and 15:00 PST (black line in Fig. 3a), following the evolution of surface wind speed (Fig. S1). Although the fallow land fraction across the CV is only 6-8 % (Fig. 1b), accounting for less than 10 % of the total irrigated land area (fallow land fraction over the irrigated land fraction; Fig. 1a), fallow croplands drive a pronounced increase in atmospheric dust loading in this event, with a cumulative dust emission of 90 t within the CV (blue line in Fig. 3a). As emissions persist, atmospheric dust loading over the CV continues to increase and reaches a maximum of about 40 t at 16:00 PST (red line in Fig. 3a).

The enhanced dust aerosol loading in FLDUST leads to perturbations in the regional radiative balance. Figures 3b and 3c show the time series of ground net downward shortwave radiation (GSW) and downward longwave radiation (GLW) integrated over the CV, respectively. During daytime, GSW in both CTRL and FLDUST exhibits a cosine-like diurnal variation associated with changes in solar zenith angle, reaching a maximum at 12:00 PST. In CTRL, the integrated GSW over the CV peaks at 30 TW (black solid line in Fig. 3b). In contrast, dust aerosols in FLDUST reduce the shortwave radiation reaching the surface, with a maximum integrated GSW over the CV of 29 TW (black dashed line in Fig. 3b). Constrained jointly by solar insolation and dust aerosol loading, the maximum difference in the integrated GSW over the CV between FLDUST and CTRL is about 2 TW around 15:00 PST (blue line in Fig. 3b). The spatial distribution of dust-induced GSW reduction closely follows the distribution of atmospheric dust loading. As emissions persist and strong winds shift southward, regions of reduced GSW progressively expand to the southern CV, with a maximum cooling rate of -100 W m^{-2} in the southern CV at 15:00 PST (Fig. S2). On average, anthropogenic dust emissions from fallow croplands lead to a GSW reduction of about 40 W m^{-2} over the CV during the dust event from 06:00 PST, October 11, to 00:00 PST, October 12, 2021 (Fig. 3d).

Compared to the shortwave response, the ground downward longwave radiative effect associated with dust aerosols is weaker and exhibits a delayed temporal evolution. As shown in Fig. 3c, the

increased dust loading in FLDUST leads to an increase in GLW relative to CTRL, reflecting increased emission of terrestrial radiation by heated air and dust aerosols near the surface due to the absorption of shortwave radiation by dust aerosols. The increase in GLW (black dashed line versus black solid line in Fig. 3c) peaks at 16:00 PST, one hour lagging the peak shortwave response. The maximum difference in the integrated GLW over the CV between FLDUST and CTRL is about 0.3 TW (blue line in Fig. 3c). The spatial distribution of the longwave radiative effect is similar to that of the shortwave response (Fig. 3d versus 3e). As strong winds and dust emissions shift southward, regions of increased GLW progressively expand to the southern CV, with a maximum warming rate of 20 W m^{-2} at 16:00 PST (Fig. S3). The average GLW increase in FLDUST, compared to CTRL, is about 10 W m^{-2} during the dust event (Fig. 3e). Although the longwave warming partially offsets the shortwave cooling, its magnitude is much smaller. As a result, the net surface radiative effect during the dust event is dominated by the shortwave cooling, leading to a maximum 2-m temperature reduction of 0.5 ℃ in the southern CV at 17:00 PST (Fig. S4). And the averaged 2-m temperature reduction is about 0.2 ℃ during the dust event (Fig. 3f).

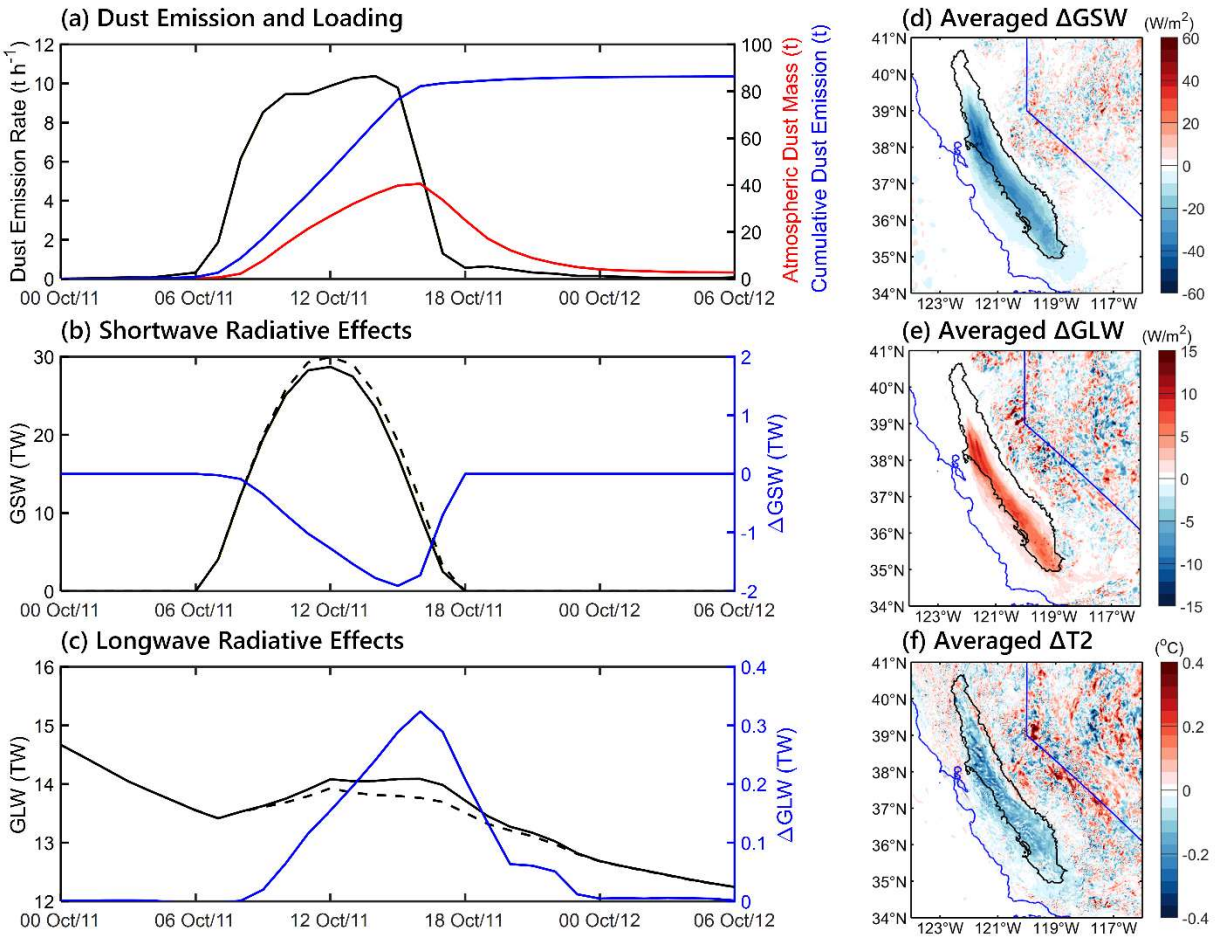

Figure 3. Time series of (a) total dust emission rate (black), atmospheric dust mass (red), and cumulative dust emission (blue); (b) simulated total net downward shortwave radiation at the surface; and (c) simulated total downward longwave radiation at the surface during the October 2021 wind event within the CV. Panels (d-f) show the spatial distribution of differences in (d) net downward shortwave radiation, (e) downward longwave radiation, and (f) 2-m temperature between FLDUST and CTRL, averaged from 06:00 PST 11 October to 00:00 PST 12 October. Solid lines in (b) and (c) denote the FLDUST experiment, while dashed lines denote the CTRL experiment. Blue lines in (b) and (c) indicate the differences between FLDUST and CTRL.

3.3 Vertical Structure of the Dust Plume and Its Impacts on Visibility

The increased dust aerosol loading in FLDUST leads to severe visibility degradation across the CV. To quantify this effect, dust-induced visibility is estimated using the following Koschmieder formula (Israël & Kasten, 1959):

$$VIS_{dust} = \frac{3.912}{\beta_{ext,dust}} \quad (3)$$

where VIS_{dust} is the visibility distance (m) associated with dust aerosols, and $\beta_{ext,dust}$ is the dust aerosol extinction coefficient with a unit of m^{-1}. In the WRF-Chem model, the dust extinction coefficient is calculated as $\beta_{ext,dust} = \rho \sum_{n=1}^{5} a_n D_n$, where ρ is air density, D_n is the mixing ratio of dust aerosols in the nth dust size bin, and a_n is the mass extinction efficiency coefficient for each dust size bin.

Figure 4 shows the latitude-height cross-sections of dust aerosol distribution, radiative effects, and visibility reduction over the CV during the October 11, 2021, dust event. The vertical distribution of dust aerosols (black contours in Fig. 4) reflects strong surface emissions from fallow croplands, boundary layer mixing, sedimentation, and turbulent mixing driven by synoptic-scale wind extremes. The dust plume is primarily constrained within the lower atmosphere below 3 km, with the highest concentrations near the surface that decrease rapidly with height. Thus, fallow-land-emitted dust aerosols induce pronounced vertical gradients in radiative effects. Dust aerosols enhance shortwave radiative heating in the lower atmosphere (Fig. 4b), while the associated decrease in longwave radiative heating is weaker (Fig. 4c), resulting in a net heating tendency (Fig. 4a). Although dust-induced radiative heating in the lower atmosphere tends to increase instability and favor dust dispersion, dust aerosols also reduce the net shortwave radiation reaching the surface through absorption and scattering, leading to surface cooling (Fig. 3f). This dust-induced surface cooling reduces sensible heat fluxes (Fig. S5) and suppresses boundary layer growth, as evidenced by the reduced planetary boundary layer height (PBLH; Fig. S6), indicating that the surface cooling effect dominates the destabilization of dust-induced radiative heating. As a result, turbulent mixing is suppressed, retaining dust aerosols near the surface and limiting their long-range transport. High dust concentration enhances aerosol extinction, while reduced turbulent mixing limits vertical dispersion, together leading to severe visibility degradation. During the October 11, 2021, dust event, the most pronounced visibility reduction occurred in the southern CV, where dust loading is high. The visibility is reduced by 900-1000 m between FLDUST and CTRL, consistent with the accumulation of dust over that region (Fig. 4d).

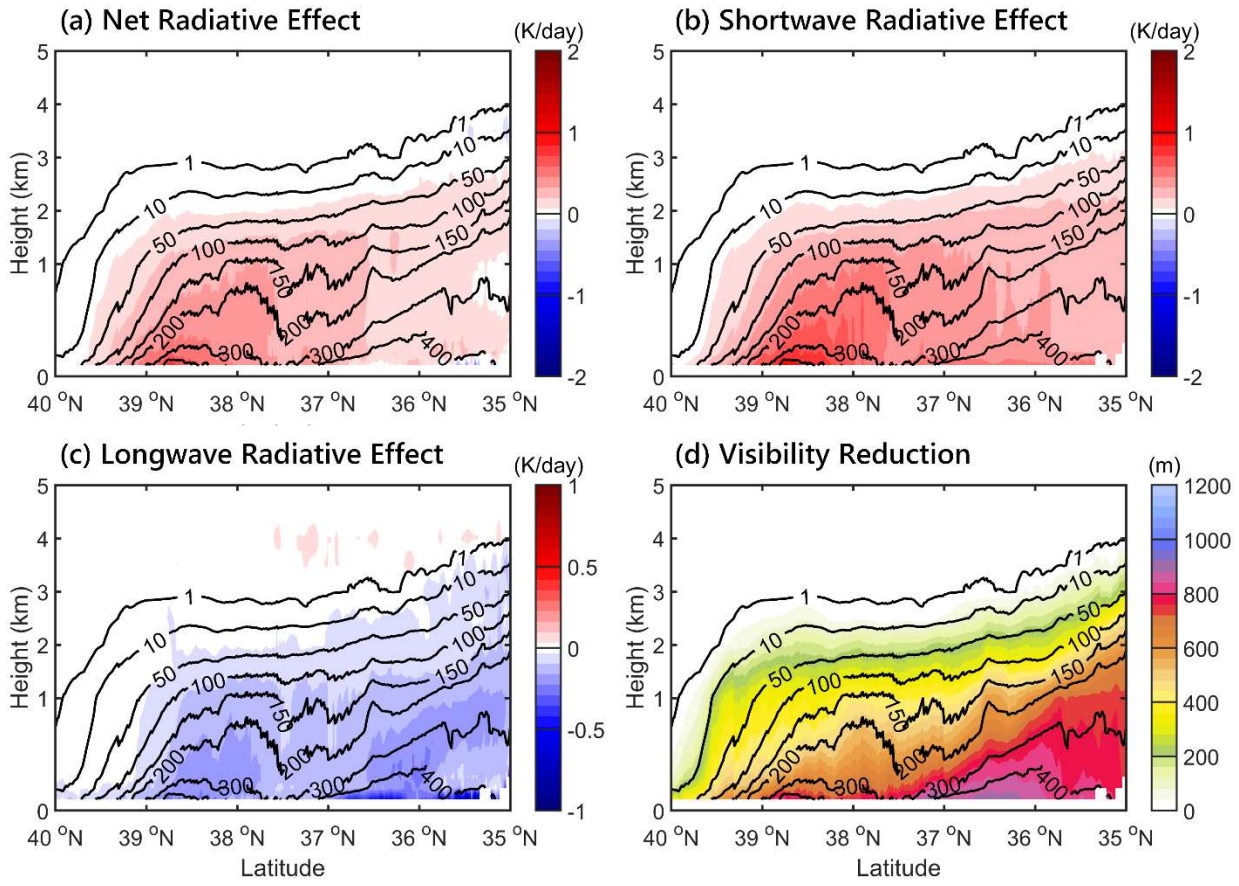

Figure 4. Latitude-height cross section of (a) net radiative effect, (b) shortwave radiative effect, (c) longwave radiative effect, and (d) visibility reduction due to dust over California's Central Valley during the October 2021 wind event. Shading shows the dust-induced changes between FLDUST and CTRL. Black contours are dust mixing ratio (total dust; sum of dust size bins 1-5) in FLDUST (μg kg^{-1}). Values in the figure are averaged from 06:00 PST 11 October to 00:00 PST 12 October.

4. Summary and Conclusions

This study investigates the role of fallow croplands in driving anthropogenic dust emissions during the October 11, 2021, wind-driven dust event over California's CV using 1.3-km-resolution WRF-Chem simulations. By incorporating satellite-derived fallow land fractions into the AFWA dust emission scheme, the WRF-Chem model explicitly represents exposed fallow croplands that can emit dust under strong winds. The control simulation (CTRL), which uses the default AFWA

erodibility, produces little dust aerosol loading and fails to reproduce the observed dust event over the CV. In contrast, the experiment including fallow-cropland-induced erodibility (FLDUST) generates substantial dust emissions, with a cumulative dust emission of 90 t within the CV during the event, and successfully reproduces the observed AOD of 0.6-0.8 and PM_{10} concentrations of 1000-1200 μg m^{-3} across the CV. Although fallow croplands account for less than 10 % of the agricultural land area in the CV, they can produce large amounts of windblown dust and become a dominant anthropogenic dust source during the October 2021 dust event.

Dust emissions from fallow croplands in FLDUST significantly increase atmospheric dust loading over the CV and lead to clear impacts on surface radiation and visibility. Dust aerosols emitted from fallow croplands reduce net downward shortwave radiation (GSW) integrated over the CV by about 2 TW at 15:00 PST and increase downward longwave radiation (GLW) by about 0.3 TW at 16:00 PST. The net radiative effect is dominated by shortwave cooling, leading to near-surface cooling of 0.5 ℃ in FLDUST, compared to CTRL, in the southern CV. The dust plume is mainly confined to the lower atmosphere below 3 km and causes a strong reduction in visibility near the surface, with the largest reduction of 900-1000 m over the southern CV. These results confirm that fallow croplands can become a major anthropogenic dust source and significantly affect air quality, the radiation budget, and near-surface visibility during strong wind events.

Our results linking agricultural fallowing to extreme visibility degradation during the October 11, 2021, dust event in California's CV have broader implications that may be influenced by changes in California climate and policy. Specifically, the disproportionate contribution of a relatively small fallow land area to regional dust emissions and visibility degradation suggests that future changes in both drought frequency and agricultural water policy could substantially alter the magnitude and frequency of anthropogenic dust events across the CV. For example, projected warming and drying trends across California are expected to intensify drought conditions throughout the 21st century, increasing the frequency and severity of multi-year droughts (Cook et al., 2015; Legg, 2021). These trends are particularly relevant to the CV, where soil moisture deficits and reduced vegetation cover during drought years directly increase the surface erodibility of agricultural lands. Under future warming scenarios, drought-driven fallowing episodes are projected to become more frequent and spatially extensive, suggesting that anthropogenic dust events of the kind documented here may become increasingly common (Gebremichael et al., 2021; Liu et al., 2022; Marston &

Konar, 2017; Stewart et al., 2020). Furthermore, the coupling between drought, fallowing, and dust emissions represents positive feedback: dust aerosols reduce surface shortwave radiation and suppress boundary layer mixing, potentially modifying regional precipitation patterns, snowpack melting, and further reducing water availability.

In addition, the Sustainable Groundwater Management Act (SGMA), enacted in California in 2014, mandates that groundwater basins across the state achieve groundwater sustainability by 2040 (Ayres et al., 2022). In the CV, where groundwater overdraft has historically subsidized irrigated agriculture lands during dry years, SGMA implementation is expected to result in substantial reductions in groundwater pumping, forcing widespread fallowing of irrigated croplands that can no longer be supported by sustainable water allocations (Escriva-Bou et al., 2026). Projections suggest that SGMA-driven fallowing could remove hundreds of thousands of hectares of previously irrigated cropland from active production over the coming decades (Hanak et al., 2019), creating persistent, spatially extensive areas of exposed, erodible soil. Our results demonstrate that even a fallow land fraction of 6-8% of total irrigated area is sufficient to drive extreme dust emissions and PM_{10} concentrations exceeding 1000 $\mu g\ m^{-3}$ during strong wind events. As SGMA-driven fallowing expands the spatial footprint of erodible surfaces beyond the drought-driven levels observed in 2021, the risk of severe anthropogenic dust events, and their associated air quality, visibility, and public health consequences, is likely to increase substantially. This underscores the urgent need to incorporate dynamic, policy-informed representations of fallow land fractions into regional air quality forecasting and dust emission modeling frameworks, and to develop coordinated land management strategies that mitigate dust emission risks on fallowed lands, such as cover cropping, conservation tillage, and windbreak installation.

Acknowledgments

A.A.A acknowledges support from the Hellman Fellowship awarded by the University of California and the San Joaquin Valley Climate Resilience Center from the Department of Energy (Award # DE-SC0024238). S.-H. Chen acknowledges support from NASA Weather and Atmospheric Dynamics Program Award 80NSSC20K0906.

Data Availability Statement

The WRF-Chem version 4.6.1 model is available from the National Center for Atmospheric Research's (NCAR) public WRF-Model Release page on GitHub at https://github.com/wrf-model/WRF/releases. ERA5 reanalysis data are available from the Copernicus Climate Change Service (C3S) Climate Data Store (CDS). The hourly ERA5 pressure-level data are available at https://doi.org/10.24381/cds.bd0915c6, and the hourly ERA5 single-level data are available at https://doi.org/10.24381/cds.adbb2d47. The CDL data are available from USDA website at https://www.nass.usda.gov/Research_and_Science/Cropland/Release/index.php. The NDVI from Landsat-8 satellite are available from the USGS website at https://www.usgs.gov/landsat-missions/landsat-normalized-difference-vegetation-index. The NWS ASOS data are available from the NOAA National Centers for Environmental Information (NCEI) website at https://www.ncei.noaa.gov/products/land-based-station/automated-surface-weather-observing-systems. The AOD from Terra and Aqua MODIS and Suomi NPP and NOAA-20 VIIRS observations are available from the National Aeronautics and Space Administration (NASA) Level-1 and Atmosphere Archive and Distribution System Distributed Active Archive Center (LAADS DAAC) website at https://ladsweb.modaps.eosdis.nasa.gov. And the hourly EPA PM_{10} observations are available at https://aqs.epa.gov/aqsweb/airdata/download_files.html#Raw.

Reference

Adebiyi, A. A., Kibria, Md. M., Abatzoglou, J. T., Ginoux, P., Pandey, S., Heaney, A., et al. (2025). Fallowed agricultural lands dominate anthropogenic dust sources in California. *Communications Earth & Environment*, *6*(1), 324. https://doi.org/10.1038/s43247-025-02306-0

Ayres, A., Kwon, J., & Collins, J. (2022). *Land Transitions and Dust in the San Joaquin Valley How Proactive Management Can Support Air Quality Improvements*.

Baddock, M. C., Ginoux, P., Bullard, J. E., & Gill, T. E. (2016). Do MODIS-defined dust sources have a geomorphological signature? *Geophysical Research Letters*, *43*(6), 2606–2613. https://doi.org/10.1002/2015GL067327

Baker, J. B., Southard, R. J., & Mitchell, J. P. (2005). Agricultural Dust Production in Standard and Conservation Tillage Systems in the San Joaquin Valley. *Journal of Environmental Quality*, *34*(4), 1260–1269. https://doi.org/10.2134/jeq2003.0348

Bhattachan, A., Okin, G. S., Zhang, J., Vimal, S., & Lettenmaier, D. P. (2019). Characterizing the Role of Wind and Dust in Traffic Accidents in California. *GeoHealth*, *3*(10), 328–336. https://doi.org/10.1029/2019GH000212

Centers for Disease Control and Prevention (CDC). (2013). Increase in reported coccidioidomycosis--United States, 1998-2011. *MMWR. Morbidity and Mortality Weekly Report*, *62*(12), 217–21. Retrieved from http://www.ncbi.nlm.nih.gov/pubmed/23535687

Chen, S., Chen, J., Zhang, Y., Lin, J., Bi, H., Song, H., et al. (2023). Anthropogenic dust: sources, characteristics and emissions. *Environmental Research Letters*, *18*(10), 103002. https://doi.org/10.1088/1748-9326/acf479

Cook, B. I., Ault, T. R., & Smerdon, J. E. (2015). Unprecedented 21st century drought risk in the American Southwest and Central Plains. *Science Advances*, *1*(1). https://doi.org/10.1126/sciadv.1400082

Cooksey, G. L. S., Nguyen, A., Duc Vugia, ;, & Jain, S. (2020). *Morbidity and Mortality Weekly Report Regional Analysis of Coccidioidomycosis Incidence-California, 2000-2018*. Retrieved from https://www.cdc.gov/nchs/data/statnt/statnt20.pdf.

Dominski, F. H., Lorenzetti Branco, J. H., Buonanno, G., Stabile, L., Gameiro da Silva, M., & Andrade, A. (2021). Effects of air pollution on health: A mapping review of systematic reviews and meta-analyses. *Environmental Research*, *201*, 111487. https://doi.org/10.1016/j.envres.2021.111487

Ebiendele, P., Adebiyi, A., Abatzoglou, J., Ardon-Dryer, K., Kibria, M. M., & Hogle, C. (2026, March 11). Characterization and Meteorological Drivers of Dust Events over California's Central Valley. https://doi.org/10.31223/X53193

Escriva-Bou, A., Hanak, E., Cole, S., & Medellín-Azuara, J. (2026). *Water challenges loom over California's most important farming region*.

Espinoza, V., Bernacchi, L. A., Eriksson, M., Schiller, A., Hayden, A., & Viers, J. H. (2023). From fallow ground to common ground: Perspectives on future land uses in the San Joaquin valley under sustainable groundwater management. *Journal of Environmental Management*, *333*, 117226. https://doi.org/10.1016/j.jenvman.2023.117226

Evans, S., Ginoux, P., Malyshev, S., & Shevliakova, E. (2016). Climate-vegetation interaction and amplification of Australian dust variability. *Geophysical Research Letters*, *43*(22), 11,823-11,830. https://doi.org/10.1002/2016GL071016

Gebremichael, M., Krishnamurthy, P. K., Ghebremichael, L. T., & Alam, S. (2021). What Drives Crop Land Use Change during Multi-Year Droughts in California's Central Valley? Prices or Concern for Water? *Remote Sensing*, *13*(4), 650. https://doi.org/10.3390/rs13040650

Ginoux, P., Garbuzov, D., & Hsu, N. C. (2010). Identification of anthropogenic and natural dust sources using Moderate Resolution Imaging Spectroradiometer (MODIS) Deep Blue level 2 data. *Journal of Geophysical Research: Atmospheres*, *115*(D5). https://doi.org/10.1029/2009JD012398

Ginoux, P., Prospero, J. M., Gill, T. E., Hsu, N. C., & Zhao, M. (2012). Global-scale attribution of anthropogenic and natural dust sources and their emission rates based on MODIS Deep Blue aerosol products. *Reviews of Geophysics*, *50*(3), 1–36. https://doi.org/10.1029/2012RG000388

Goudie, A. S. (2014). Desert dust and human health disorders. *Environment International*, *63*, 101–113. https://doi.org/10.1016/j.envint.2013.10.011

Hanak, E., Escriva-Bou, A., Gray, B., Green, S., Harter, T., Jezdimirovic, J., et al. (2019). *Water and the Future of the San Joaquin Valley OVERVIEW*.

Hsu, N. C., Jeong, M. -J., Bettenhausen, C., Sayer, A. M., Hansell, R., Seftor, C. S., et al. (2013). Enhanced Deep Blue aerosol retrieval algorithm: The second generation. *Journal of Geophysical Research: Atmospheres*, *118*(16), 9296–9315. https://doi.org/10.1002/jgrd.50712

Huang, J. P., Liu, J. J., Chen, B., & Nasiri, S. L. (2015). Detection of anthropogenic dust using CALIPSO lidar measurements. *Atmospheric Chemistry and Physics*, *15*(20), 11653–11665. https://doi.org/10.5194/acp-15-11653-2015

Israël, H., & Kasten, F. (1959). KOSCHMIEDERs Theorie der horizontalen Sichtweite. In *Die Sichtweite im Nebel und die Möglichkeiten ihrer künstlichen Beeinflussung* (pp. 7–10). Wiesbaden: VS Verlag für Sozialwissenschaften. https://doi.org/10.1007/978-3-663-04661-5_2

Kok, J., Gupta, A., Evan, A., Adebiyi, A., Albani, S., Balkanski, Y., et al. (2025, July 19). Desert dust exerts a substantial longwave radiative forcing missing from climate models. https://doi.org/10.31223/X53B2J

Kok, J. F., Storelvmo, T., Karydis, V. A., Adebiyi, A. A., Mahowald, N. M., Evan, A. T., et al. (2023). Mineral dust aerosol impacts on global climate and climate change. *Nature Reviews Earth & Environment*, *4*(2), 71–86. https://doi.org/10.1038/s43017-022-00379-5

Legg, S. (2021). IPCC, 2021: Climate Change 2021 - the Physical Science basis. *Interaction*, *49*(4), 44–45. Retrieved from https://search.informit.org/doi/10.3316/informit.315096509383738

LeGrand, S. L., Polashenski, C., Letcher, T. W., Creighton, G. A., Peckham, S. E., & Cetola, J. D. (2019). The AFWA dust emission scheme for the GOCART aerosol model in WRF-Chem v3.8.1. *Geoscientific Model Development*, *12*(1), 131–166. https://doi.org/10.5194/gmd-12-131-2019

Liu, P.-W., Famiglietti, J. S., Purdy, A. J., Adams, K. H., McEvoy, A. L., Reager, J. T., et al. (2022). Groundwater depletion in California's Central Valley accelerates during megadrought. *Nature Communications*, *13*(1), 7825. https://doi.org/10.1038/s41467-022-35582-x

Mahowald, N. M., & Luo, C. (2003). A less dusty future? *Geophysical Research Letters*, *30*(17). https://doi.org/10.1029/2003GL017880

Marston, L., & Konar, M. (2017). Drought impacts to water footprints and virtual water transfers of the <scp>C</scp> entral <scp>V</scp> alley of <scp>C</scp> alifornia. *Water Resources Research*, *53*(7), 5756–5773. https://doi.org/10.1002/2016WR020251

Marticorena, B., & Bergametti, G. (1995). Modeling the atmospheric dust cycle: 1. Design of a soil-derived dust emission scheme. *Journal of Geophysical Research*, *100*(D8). https://doi.org/10.1029/95jd00690

Miller, R. L., & Tegen, I. (1998). Climate Response to Soil Dust Aerosols. *Journal of Climate*, *11*(12), 3247–3267. https://doi.org/10.1175/1520-0442(1998)011<3247:CRTSDA>2.0.CO;2

Ostro, B., Awe, Y., & Sánchez-Triana, E. (2021). *When the Dust Settles: A Review of the Health Implications of the Dust Component of Air Pollution*. Retrieved from www.worldbank.org

Philip, S., Martin, R. V, Snider, G., Weagle, C. L., van Donkelaar, A., Brauer, M., et al. (2017). Anthropogenic fugitive, combustion and industrial dust is a significant, underrepresented fine particulate matter source in global atmospheric models. *Environmental Research Letters*, *12*(4), 044018. https://doi.org/10.1088/1748-9326/aa65a4

Plassin, S., Koch, J., Wilson, M., Neal, K., Friedman, J. R., Paladino, S., & Worden, J. (2021). Multi-scale fallow land dynamics in a water-scarce basin of the U.S. Southwest. *Journal of Land Use Science*, *16*(3), 291–312. https://doi.org/10.1080/1747423X.2021.1928310

Prospero, J. M., Ginoux, P., Torres, O., Nicholson, S. E., & Gill, T. E. (2002). ENVIRONMENTAL CHARACTERIZATION OF GLOBAL SOURCES OF ATMOSPHERIC SOIL DUST IDENTIFIED WITH THE NIMBUS 7 TOTAL OZONE MAPPING SPECTROMETER (TOMS) ABSORBING AEROSOL PRODUCT. *Reviews of Geophysics*, *40*(1), 2-1-2–31. https://doi.org/10.1029/2000RG000095

Pu, B., Jin, Q., Ginoux, P., & Yu, Y. (2022). Compound Heat Wave, Drought, and Dust Events in California. *Journal of Climate*, *35*(24), 8133–8152. https://doi.org/10.1175/JCLI-D-21-0889.1

Shevliakova, E., Malyshev, S., Martinez-Cano, I., Milly, P. C. D., Pacala, S. W., Ginoux, P., et al. (2024). The Land Component LM4.1 of the GFDL Earth System Model ESM4.1: Model Description and Characteristics of Land Surface Climate and Carbon Cycling in the Historical Simulation. *Journal of Advances in Modeling Earth Systems*, *16*(5). https://doi.org/10.1029/2023MS003922

Stanelle, T., Bey, I., Raddatz, T., Reick, C., & Tegen, I. (2014). Anthropogenically induced changes in twentieth century mineral dust burden and the associated impact on radiative forcing. *Journal of Geophysical Research: Atmospheres*, *119*(23), 13,526-13,546. https://doi.org/10.1002/2014JD022062

Stewart, I. T., Rogers, J., & Graham, A. (2020). Water security under severe drought and climate change: Disparate impacts of the recent severe drought on environmental flows and water supplies in Central California. *Journal of Hydrology X*, *7*, 100054. https://doi.org/10.1016/j.hydroa.2020.100054

Tegen, I., & Fung, I. (1995). Contribution to the atmospheric mineral aerosol load from land surface modification. *Journal of Geophysical Research: Atmospheres*, *100*(D9), 18707–18726. https://doi.org/10.1029/95JD02051

Tong, D., Feng, I., Gill, T. E., Schepanski, K., & Wang, J. (2023). How Many People Were Killed by Windblown Dust Events in the United States? *Bulletin of the American Meteorological Society*, *104*(5), E1067–E1084. https://doi.org/10.1175/BAMS-D-22-0186.1

Tong, D. Q., Wang, J. X. L., Gill, T. E., Lei, H., & Wang, B. (2017). Intensified dust storm activity and Valley fever infection in the southwestern United States. *Geophysical Research Letters*, *44*(9), 4304–4312. https://doi.org/10.1002/2017GL073524

Webb, N. P., & Pierre, C. (2018, February 1). Quantifying Anthropogenic Dust Emissions. *Earth's Future*. John Wiley and Sons Inc. https://doi.org/10.1002/2017EF000766

Xi, X., & Sokolik, I. N. (2016). Quantifying the anthropogenic dust emission from agricultural land use and desiccation of the Aral Sea in Central Asia. *Journal of Geophysical Research: Atmospheres*, *121*(20), 12,270-12,281. https://doi.org/10.1002/2016JD025556

Zender, C. S., Miller, R. L. R. L., & Tegen, I. (2004). Quantifying mineral dust mass budgets:Terminology, constraints, and current estimates. *Eos, Transactions American Geophysical Union*, *85*(48), 509–512. https://doi.org/10.1029/2004EO480002